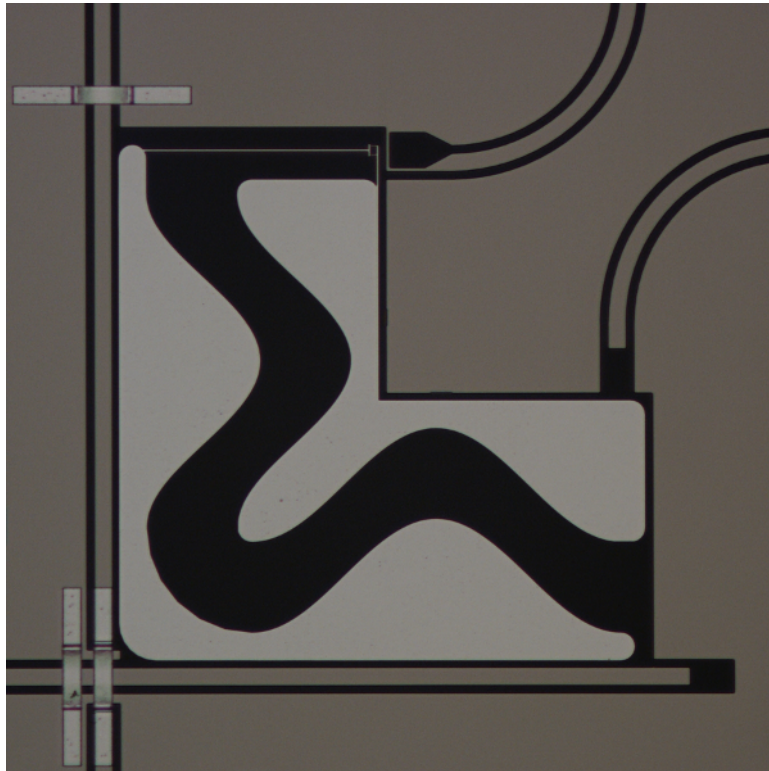


Optimization of transmon design for longer coherence time

Simon Burkhard

Semester thesis
Spring semester 2012

Supervisor: Dr. Arkady Fedorov



ETH Zurich
Quantum Device Lab
Prof. Dr. A. Wallraff

Abstract

Using electrostatic simulations, a transmon qubit with new shape and a large geometrical size was designed. The coherence time of the qubits was increased by a factor of 3-4 to about $4 \mu\text{s}$. Additionally, a new formula for calculating the coupling strength of the qubit to a transmission line resonator was obtained, allowing reasonably accurate tuning of qubit parameters prior to production using electrostatic simulations.

Contents

1	Introduction	4
2	Theory	5
2.1	Coplanar waveguide resonator	5
2.1.1	Quantum mechanical treatment	5
2.2	Superconducting qubits	5
2.2.1	Cooper pair box	6
2.2.2	Transmon	7
2.3	Resonator-qubit coupling (Jaynes-Cummings model)	9
2.4	Effective transmon network	9
2.4.1	Calculation of C_Σ	10
2.4.2	Calculation of β	10
2.4.3	Qubits coupled to 2 resonators	11
2.4.4	Charge line and flux line couplings	11
2.5	Transmon relaxation time (T_1)	11
3	Transmon simulation	12
3.1	Ansoft Maxwell	12
3.1.1	Convergence of simulations	13
3.1.2	Field integral	13
3.2	Optimization of transmon parameters	14
3.3	Intermediate transmon design	15
3.4	Final transmon design	15
3.5	Comparison of the surface electric field	17
3.6	Simple estimate of T_1 due to coupling to the charge line	17
3.7	Simulation of the magnetic flux through the split junction	18
4	Conclusion and outlook	19
A	Additional tables	20
B	Additional figures	21
C	List of simulation files	23
D	Maxwell "manual"	24
D.1	General	24
D.2	Import and export CAD drawings	24
D.3	Excitations, Matrix, Solution Setup	24
D.4	Output variables, field calculator, reports	25
D.5	Design Parameters	25
D.6	Magnetostatic solution	26

1 Introduction

In the past decades, scientists have developed growing interest in experimental realizations of quantum information processing. The development of a computer consisting of quantum bits (qubits), which possess an infinite number of continuous superposition states in contrast to a classical bit with only two states, could lead to a tremendous increase in computational power for certain problems [1].

A promising type of qubit for the realization of a quantum computer is the transmon [2], which consists of two superconducting islands connected by Josephson junctions. This type of qubit can be fabricated reliably using modern lithography techniques, which are well-established fabrication methods, allowing to specifically design some properties of the qubit. In particular, such qubits have a macroscopic size, leading to a dipole moment which is larger by orders of magnitude than the dipole moment of e.g. atoms, allowing strong coupling to electric fields for qubit manipulation and transport of information from one qubit to another using photons.

Unfortunately, the possibilities of transmon manipulation are currently limited by their relaxation time (T_1) and dephasing time (T_2). In this semester project, a new transmon design with an increased overall size was introduced, leading to an increase of the relaxation time by a factor of 3-4. Initially, simulations for the important qubit parameters E_C and g were validated using existing qubit designs. As a second step, qubits with an intermediate size were designed, leading to an increase in coherence time already. Finally, a new design of large transmons was introduced, but the coherence time remained roughly the same as with the intermediate size.

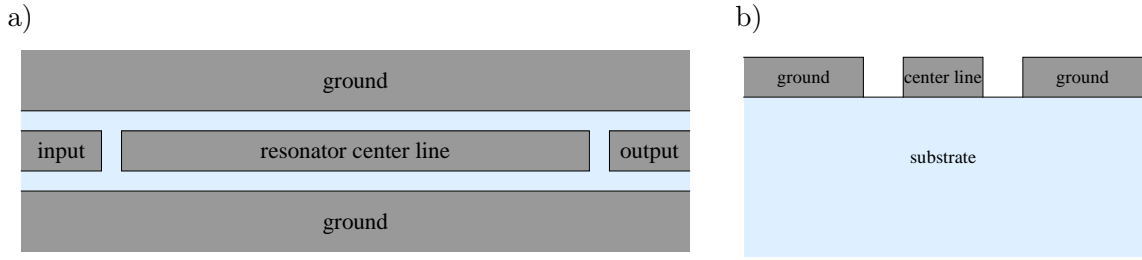


Figure 2.1: a) Top view of a simple coplanar waveguide resonator. b) Cross section of a CPW. Note that the dimensions are not to scale.

2 Theory

In this section, the fundamental theory underlying the operation of transmon qubits will be introduced, closely following ref. [3] unless mentioned otherwise.

2.1 Coplanar waveguide resonator

A 1D coplanar waveguide resonator (CPW), shown in Fig. 2.1, consists of a center conduction line separated from coplanar ground planes by a gap. Input and output transmission lines are coupled capacitively to the resonator line. The conductors consist of thin layers of conducting material mounted on an isolating substrate in a photo-lithographic process.

The fundamental mode of a CPW of length l is given by the standing wave resonance condition at a wavelength $\lambda = 2l$. This is the relevant mode for the interaction between the resonator and the qubit if the qubit is placed at an end of the resonator.

2.1.1 Quantum mechanical treatment

A superconducting CPW resonator can be modeled by a simple parallel LC oscillator (inductance L_r , capacitance C_r) carrying a current $I(t)$ and a voltage drop $v(t)$. According to ref. [4], a Hamiltonian formulation of a circuit requires the flux $\Phi(t) = \int_{-\infty}^t v(t') dt'$ and the charge $Q(t) = \int_{-\infty}^t I(t') dt'$. Replacing these quantities by their corresponding quantum mechanical operators $\hat{\phi}$ and q , obeying the commutation relations $[\hat{\phi}, q] = i\hbar$, the quantum mechanical Hamiltonian of the system can be written as

$$H_{res} = \frac{q^2}{2C_r} + \frac{\phi^2}{2L_r} = \hbar\omega_r \left(a^\dagger a + \frac{1}{2} \right), \quad (2.1)$$

with the angular resonance frequency $\omega_r = 1/\sqrt{L_r C_r}$, the characteristic impedance $Z = \sqrt{L_r/C_r}$ and $a = \frac{1}{\sqrt{2\hbar Z}}(\hat{\phi} + iZq)$ obeying $[a, a^\dagger] = 1$.

2.2 Superconducting qubits

In contrast to a classical bit, which can only assume two values 0 or 1, a qubit (quantum bit) is a quantum mechanical system described by a two-dimensional Hilbert space with two basis states $|0\rangle$ and $|1\rangle$, i.e. it can assume a continuum of states $|\Psi\rangle = \alpha|0\rangle + \beta|1\rangle$ with $|\alpha|^2 + |\beta|^2 = 1$. Superconducting qubits have a large number of eigenstates, so in order to induce transitions between two states only, the energy spectrum of the qubit needs to be sufficiently anharmonic. Typically, the ground state $|g\rangle$ and the first excited state $|e\rangle$ of the qubit will be the states of choice, since the ground state can be initialized reliably if $k_B T \ll E_e - E_g = \hbar\nu_{ge}$. To

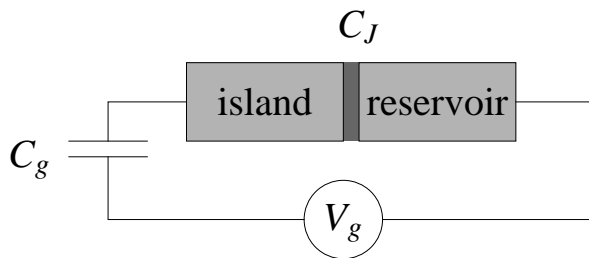


Figure 2.2: Schematic drawing of a Cooper pair box qubit. A superconducting island is connected to a superconducting reservoir by a Josephson tunnel junction with capacitance C_J (typical value: 6 fF). An external gate Voltage V_g is applied between the superconductors via a capacitance C_g , inducing a charge difference $C_g V_g$. A charge imbalance between the superconductors results depending on V_g , because charge can only tunnel across the junction in units of Cooper pairs.

perform operations on the qubit, these states need to be sufficiently long-lived compared to the manipulation time.

2.2.1 Cooper pair box

The Cooper pair box (CPB) was the first qubit based on superconducting circuits [5, 6]. It consists of a superconducting island connected to a superconducting reservoir by a Josephson tunnel junction, as shown in Fig. 2.2. The Josephson junction consists of two superconductors connected by a very thin layer (on the order of 1 nm) of insulating material, allowing Cooper pairs to tunnel between the superconductors without transmission of quasiparticles [7].

The Hamiltonian of the CPB is given as [2]

$$H_{qb} = 4E_C(\hat{n} - n_g)^2 - E_J \cos \hat{\varphi}. \quad (2.2)$$

$n_g = Q_r/2e + C_g V_g/2e$ is the induced charge difference (offset charge), where Q_r is some environment-induced charge difference and $C_g V_g$ is the induced charge difference due to the external voltage as defined in Fig. 2.2. \hat{n} denotes the number of Cooper pairs transferred between the islands and $\hat{\varphi}$ is the gauge-invariant phase difference between the superconductors. Note that both \hat{n} and n_g are measured in units of $2e$ (Cooper pairs).

$$E_C = \frac{e^2}{2C_\Sigma} \quad (2.3)$$

is the charging energy required to put an additional electron on the island, where C_Σ is the total capacitance between the superconductors. The Josephson energy E_J is the coupling energy associated with the tunneling of one electron across the junction. To illustrate this in a different notation, the Hamiltonian can also be written in the basis of eigenstates $|n\rangle$ of the Cooper pair number operator, i.e. $\hat{n}|n\rangle = n|n\rangle$, as used in ref. [6]:

$$H_{qb} = 4E_C \sum_n (n - n_g)^2 |n\rangle\langle n| - E_J \sum_n (|n\rangle\langle n+1| + |n+1\rangle\langle n|). \quad (2.4)$$

Moreover, this form of the Hamiltonian can approximately be solved numerically by diagonalization if a truncated basis of $2N + 1$ states $|n\rangle$, $n = -N, \dots, N$ is used.

For a simple CPB, as shown schematically in Fig. 2.2, the Josephson energy E_J is a constant, determined by design parameters and material properties of the Josephson junction. However, by designing a qubit with a split junction, i.e. two spatially separated junctions forming a

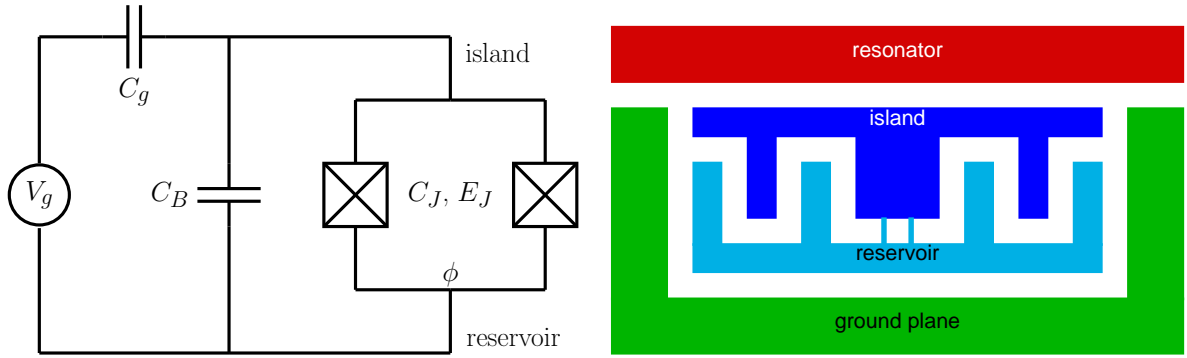


Figure 2.3: left: Effective circuit diagram of the transmon qubit. The island and the reservoir are coupled via an additional effective capacitance C_B , increasing the total capacitance $C_\Sigma = C_B + C_J + C_g$ between the superconductors w.r.t. the CPB. ϕ denotes the magnetic flux through the split junction loop. right: schematic of a simple transmon design.

superconducting loop, the Josephson energy E_J can be tuned by applying an external magnetic field inducing a magnetic flux ϕ through the loop:

$$E_J(\phi) = E_{J_{max}} \left| \cos \left(\frac{\pi\phi}{\phi_0} \right) \right|, \quad (2.5)$$

where ϕ_0 is the magnetic flux quantum and $E_{J_{max}}$ a constant, depending again on the fabrication parameters of the junctions.

2.2.2 Transmon

The transmon (transmission-line shunted plasma oscillation qubit) is an advanced qubit design based on the Cooper pair box. In contrast to the CPB, the island and the reservoir are capacitively coupled to each other with a much larger additional (effective) capacitance C_B than the junction capacitance C_J , increasing C_Σ and therefore reducing E_C . The effective capacitance network of the transmon network is shown in Fig. 2.3. Analogous to the CPB, the external gate voltage V_g could in principle be used to control the offset charge $n_g = Q_r/2e + C_g V_g/2e$ of the transmon qubit.

The main advantage of the transmon compared to the simple CPB is the much higher ratio E_J/E_C . An increase of E_J/E_C leads to an exponential decrease of the charge dispersion (dependence of the eigenenergies on n_g), while the anharmonicity of the energy levels decreases with a weak power law only [2]. The first three energy levels of the transmon are shown in Fig. 2.4 as a function of n_g for different ratios E_J/E_C .

In the limit $E_J/E_C \gg 1$, the transmon Hamiltonian can be solved approximately using perturbation theory [2], leading to an analytical approximation for the energy E_m of state m :

$$E_m \approx -E_J + \sqrt{8E_C E_J} \left(m + \frac{1}{2} \right) - \frac{E_C}{12} (6m^2 + 6m + 3). \quad (2.6)$$

The resulting absolute anharmonicity is $-E_C$. In short, the transmon design strongly reduces the sensitivity to charge noise (i.e. changes in n_g), while preserving an anharmonic energy level spectrum needed for state control.

The transition frequency from the ground state to the first excited state is given as

$$\nu_{ge} \approx \frac{\sqrt{8E_J E_C} - E_C}{h}. \quad (2.7)$$

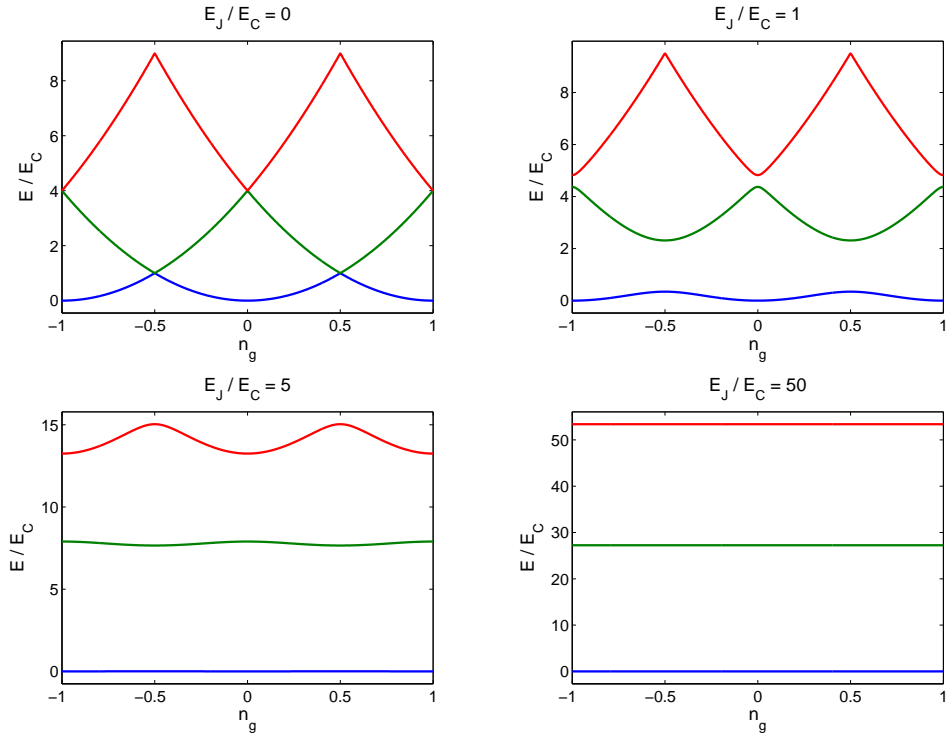


Figure 2.4: The charge dispersion of the first three eigenstates of the transmon Hamiltonian for different ratios E_J/E_C . Energies are given in units of E_C and the zero point of energy is chosen as the minimum of the lowest state. $E_J/E_C = 0$ corresponds to unperturbed pure charge eigenstates with a parabolic dispersion. In the limit $E_J \gg E_C$, the eigenenergies become independent of n_g . The energies were calculated in Matlab using Eq. (2.4) and a truncated basis of 201 basis states ($N = 100$).

2.3 Resonator-qubit coupling (Jaynes-Cummings model)

The interaction of a transmon and a CPW resonator can be described by the Jaynes-Cummings model. In order to write down the coupled Hamiltonian, it is useful to rewrite the transmon Hamiltonian (2.2) in the basis of the uncoupled transmon eigenstates $|i\rangle$:

$$H_{qb} = \hbar \sum_i \omega_i |i\rangle \langle i|, \quad (2.8)$$

where $\hbar\omega_i$ is the energy of state $|i\rangle$. Combining this expression with the Hamiltonian of the resonator (2.1) and omitting the zero point energy of the resonator, the generalized Jaynes-Cummings Hamiltonian for the coupling of the transmon to the resonator is obtained as [2]:

$$H = \hbar \sum_i \omega_i |i\rangle \langle i| + \hbar\omega_r a^\dagger a + \hbar \sum_{i,j} g_{ij} |i\rangle \langle j| (a + a^\dagger), \quad (2.9)$$

with coupling energies

$$\hbar g_{ij} = 2e\beta \sqrt{\frac{\hbar\omega_r}{2C_r}} \langle i|n|j\rangle = \hbar g_{ji}^* \quad (2.10)$$

and

$$\beta := \frac{C_g}{C_\Sigma}. \quad (2.11)$$

For large ratios E_J/E_C , the matrix element $\langle i|n|j\rangle$ leads to a relevant contribution for nearest-neighbour coupling only ($j = i \pm 1$). The rotating wave approximation can be used to eliminate the terms in Eq. (2.9) describing simultaneous excitation/deexcitation of the qubit and the resonator, leading to the effective generalized Jaynes-Cummings Hamiltonian [2]:

$$H = \hbar \sum_i \omega_i |i\rangle \langle i| + \hbar\omega_r a^\dagger a + \left(\hbar \sum_i g_{i,i+1} |i\rangle \langle i+1| a^\dagger + h.c. \right), \quad (2.12)$$

with

$$g_{i,i+1} \approx \frac{2e}{\hbar} \beta \sqrt{\frac{\hbar\omega_r}{2C_r}} \sqrt{\frac{i+1}{2}} \left(\frac{E_J}{8E_C} \right)^{1/4} \quad (2.13)$$

and $C_r = \pi/(2\omega_r Z_0)$, $Z_0 = 50\Omega$ [3].

For the excitation of the qubit from the ground state to the first excited state (i.e. $i = 0$), the coupling becomes

$$g := g_{01} \approx \frac{\sqrt{2}e}{\hbar} \beta \sqrt{\frac{\hbar\omega_r}{C_r}} \left(\frac{E_J}{8E_C} \right)^{1/4}, \quad (2.14)$$

which will be called g from now on.

2.4 Effective transmon network

An effective circuit diagram of the transmon network was shown in Fig. 2.3. The purpose of this section is to derive the effective capacitances C_g and C_B for a qubit coupled to a single resonator. Figure 2.5 shows the real capacitance network of the transmon and again the effective network. In order to calculate E_C and g , both $C_\Sigma = C_g + C_B + C_J$ and $\beta = C_g/C_\Sigma$ are needed, which can be obtained by solving a linear system of equations which is found by making use of Kirchhoff's laws.

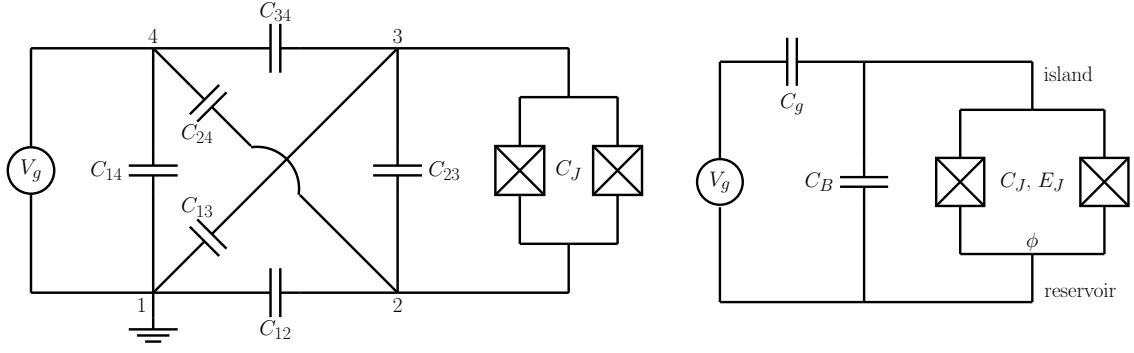


Figure 2.5: left: real capacitance network of a transmon coupled to a CPW resonator, consisting of four superconductors, i.e. ground plane (1), reservoir (2), island (3) and resonator (4). right: effective network of the transmon as described in section 2.2.2. Note that C_B can be split into $C_B = C'_B + C_{23}$.

2.4.1 Calculation of C_Σ

C_Σ is the total capacitance across the junction (between the island and the reservoir) and consists of four (effective) capacitances in parallel: $C_\Sigma = C_g + C'_B + C_{23} + C_J$, as can be seen in Fig. 2.5. C_J and C_{23} are directly determined by the transmon design, so the task is reduced to calculating $C_g + C'_B =: C_0$. This can be accomplished by replacing C_{23} and C_J in the real capacitance network by a voltage source V and calculating the total capacitance C_0 of the resulting circuit (with V_g removed). From Kirchhoff's laws, we obtain the set of equations

$$\begin{aligned}
 V &= V_{24} + V_{34} \\
 V &= V_{12} + V_{13} \\
 V &= V_{12} + V_{14} + V_{34} \\
 0 &= -Q_{12} - Q_{14} + Q_{13} \\
 0 &= Q_{14} - Q_{24} + Q_{34},
 \end{aligned}$$

which can be solved for the quantities $\{V, V_{12}, V_{13}, V_{24}, V_{34}\}$. Using $Q_{ij} = V_{ij}C_{ij}$ and the expression for the total charge

$$Q = Q_{12} + Q_{24} = Q_{13} + Q_{34} = \frac{1}{2}(Q_{12} + Q_{24} + Q_{13} + Q_{34}),$$

the capacitance C_0 is obtained as

$$C_0 = \frac{Q}{V} = \frac{(C_{12} + C_{24})(C_{13} + C_{34})}{C_{12} + C_{13} + C_{24} + C_{34}},$$

where the limit $C_{14} \rightarrow \infty$ has been taken, since the capacitance C_{14} between the resonator and the ground plane is much larger than all other capacitances (due to the much larger dimensions). Finally, C_Σ is obtained as

$$C_\Sigma = \frac{(C_{12} + C_{24})(C_{13} + C_{34})}{C_{12} + C_{13} + C_{24} + C_{34}} + C_{23} + C_J. \quad (2.15)$$

2.4.2 Calculation of β

The splitting parameter β describes the share of the voltage drop V_{23} across the junction if a gate voltage V_g is applied between ground and resonator, as in Fig. 2.5. This can easily be seen

by defining the effective shunting capacitance $C_S := C_B + C_J$. The share of the voltage drop across the junction is then given by

$$\frac{V_{23}}{V_g} = \frac{\frac{1}{C_S}}{\frac{1}{C_S} + \frac{1}{C_g}} = \frac{C_g}{C_g + C_S} = \frac{C_g}{C_\Sigma} = \beta, \quad (2.16)$$

which coincides with the definition given in Eq. (2.11). β is then obtained by using Kirchhoff's laws and solving the set of equations for the individual voltage drops. The limit $C_{14} \rightarrow \infty$ is not needed, because β does not depend on C_{14} . The final result is

$$\beta = \frac{C_{12}C_{34} - C_{13}C_{24}}{(C_{12} + C_{24})(C_{13} + C_{34}) + (C_{12} + C_{13} + C_{24} + C_{34})(C_{23} + C_J)}. \quad (2.17)$$

The detailed calculation (including the calculation of C_Σ) can be found in the file "Q:\USERS\SimonBur\Mathematica\capacitance_1res.nb"

2.4.3 Qubits coupled to 2 resonators

The procedure described above can easily be generalized to a qubit with two resonators, resulting in a larger equation system. Additionally, the capacitances between the ground plane and the resonators also have to be set to infinity in the calculation of β_1 and β_2 . Unfortunately, the resulting expressions for E_C , g_1 and g_2 get too cumbersome to fit in this report in a legible way, so they are not included, but the *Mathematica* file containing the calculation can be found at "Q:\USERS\SimonBur\Mathematica\capacitance_2res.nb".

2.4.4 Charge line and flux line couplings

As will be seen later, an actual qubit needs couplings to other electrodes for manipulation. However, these couplings are much smaller than those between island, reservoir, resonator and ground plane. Therefore, they were neglected in the calculation of C_Σ and β .

2.5 Transmon relaxation time (T_1)

As mentioned previously, the relaxation time T_1 of the excited transmon state should be long enough to perform qubit operations. A range of different processes can lead to relaxation and therefore limit T_1 [2]. It has been shown that dielectric loss from insulating materials can be a dominant source of decoherence, depending on the qubit design [8]. However, the microscopic nature of this dielectric loss is not well understood, although there are indications that the dissipation might be due to coupling to two-level fluctuators in surface impurities [9]. Ref. [10] states that for CPW resonators, the dominant contribution to the dielectric loss arises due to surface impurities in the metal-substrate and substrate-air interfaces. Therefore, reducing the electric field produced by the qubit in these surface regions seems a promising strategy for increasing T_1 . This was the main goal of this semester project.

3 Transmon simulation

Previous qubits used for measurements in our group had energy relaxation times on the order of $T_1 \sim 1 \mu\text{s}$ [11], when ref. [12] reported qubits with relaxation times on the order of $T_1 \sim 10 \mu\text{s}$. An obvious difference to our design was an increase in the overall qubit size, as illustrated in Fig. 3.1. For future experiments in our group, the charging energy E_C/h of the qubits should ideally be in a range 300 – 350 MHz and the coupling g/h between 300 – 400 MHz. So the idea was to modify the design of our qubits and see if we can get similar relaxation times, while keeping the parameters E_c and g in a similar range as before. Parallel to the beginning of this semester project, a newer transmon design had been fabricated in our group, resulting in relaxation times on the order of $4 \mu\text{s}$, but with considerably lower g on the order of 100 MHz (shown in Fig. 3.3). An overview of the properties of the different qubits is given in table A.1. For all qubit simulations, the junction capacitance was assumed to be $C_J = 6 \text{ fF}$, based on experience from previous experiments.

3.1 Ansoft Maxwell

Since the process of qubit fabrication, installation of the qubit into an experimental setup and measurement of the qubit parameters takes a long time (typically several weeks), it is not possible to just design a large set of different qubits and measure their properties in order to optimize the design. Instead, some properties of qubits can be simulated on computers. In this work, the commercial software *Ansoft Maxwell* (version 14) was used. For a user-defined qubit design, *Maxwell* numerically solves Maxwell’s equations using the iterative finite elements method. The user can define a maximum number of passes or set convergence thresholds for the simulation to end. Depending on the specific solution type chosen by the user, *Maxwell* can calculate the mutual capacitance matrix (electrostatic solution) or the mutual inductance matrix (magnetostatic solution) of the qubit superconductors. The capacitance matrix is needed to calculate E_C and g , while the inductance matrix can be useful to simulate the magnetic flux through the junction loop. In this work, the main focus was set on the simulation of E_C and g . *Maxwell* also calculates the electric (or magnetic) field at all points in the qubit model, allowing a comparison of field strengths for different qubit designs in potential problem regions for qubit relaxation. Furthermore, it is possible to define output variables as functions of both the capacitance (or inductance) matrix and field operations. After the simulation has ended, *Maxwell* will automatically calculate these output variables.

In order to create non-zero electric or magnetic fields in the qubit simulation, the user can assign so-called excitations to conductors, including voltages and charges (for an electrostatic solution) or currents (for a magnetostatic solution). In all electrostatic simulations, alternating voltages of $\pm 1 \text{ V}$ were assigned to neighbouring superconductors (and 0 V to the ground plane) so as to create field strengths which can be compared between different designs.

A very useful function of *Maxwell* for qubit optimization is the possibility to define parameters in the design, for instance the overall qubit length. *Maxwell* will then sweep this parameter over a user-defined range in steps and solve Maxwell’s equations for every step. Output variables can be stored in tables or plotted as a function of the sweep parameter, offering an efficient way of optimizing the qubit parameters with respect to systematic structural variations.

Although *Maxwell* claims to be able to deal with objects of any shape, the algorithm for creating the initial tetrahedral mesh would sometimes crash. This problem was mainly encountered while simulating objects with rectangular edges and corners (round shapes seemed less

pass	qubit a)			qubit b)		
	# tetr.	E_C/h	g/h	# tetr.	E_C/h	g/h
1	2192	6	490	11253	11	3987
2	2854	3	229	14640	15	3809
3	3711	6	255	19036	22	3053
4	4830	10	283	24749	32	2239
5	6289	12	316	32191	53	1453
6	8190	26	334	41841	81	1047
7	10673	41	455	54407	120	688
8	13892	56	394	70775	164	529
9	18067	68	397	92000	203	476
10	23475	77	332	119634	237	451
11	30498	87	285	155450	260	423
12	39657	97	278	202016	281	401
13	51543	106	248	262659	294	388
14	66971	115	233	341182	305	378
15	87106	124	219	443180	313	370
16	113202	137	180	575917	319	365
17	147240	147	171			
18	191426	158	163			
19	248848	169	152			
20	323537	177	147			
21	420618	185	142			
22	546894	193	140			

Table 3.1: Convergence of the simulation in *Maxwell* for the two qubit designs shown in Fig. 3.1. The quantities E_C/h and g/h are given in MHz. Note that the two quantities converge in opposite directions.

problematic) or objects of very different sizes. A reason for this could not be found, since the problem sometimes occurred in a parametric design variation for a few values of the parameter, while the simulation worked fine for other values, making the occurrence of the error seem random. However, sometimes, the problem could be avoided by increasing the "aspect ratio" of the tetrahedrals in the initial mesh settings (typically by a few orders of magnitude), allowing the algorithm to create tetrahedra which deviate more strongly from equilateral tetrahedra than allowed by the default settings.

3.1.1 Convergence of simulations

In table 3.1, the convergence of the quantities E_C and g is shown with respect to the number of iterations and the number of mesh tetrahedra. Since the qubit fabrication process is not precisely reproducible, i.e. fabricating the identical qubit design several times will result in qubits with slightly varying properties, it was found that the results are sufficiently converged between 500 K and 1 M mesh tetrahedra.

3.1.2 Field integral

Although the cause of the dielectric surface loss is not clear, the electric field in the surface was taken into account in the qubit optimization. In order to do so, the mean electric field (absolute value) in a 5 nm thick surface layer of the substrate was calculated by integrating the magnitude of the field over the surface layer and dividing by its volume. The extension of this layer is illustrated in Fig. 3.1 as a gray shading.

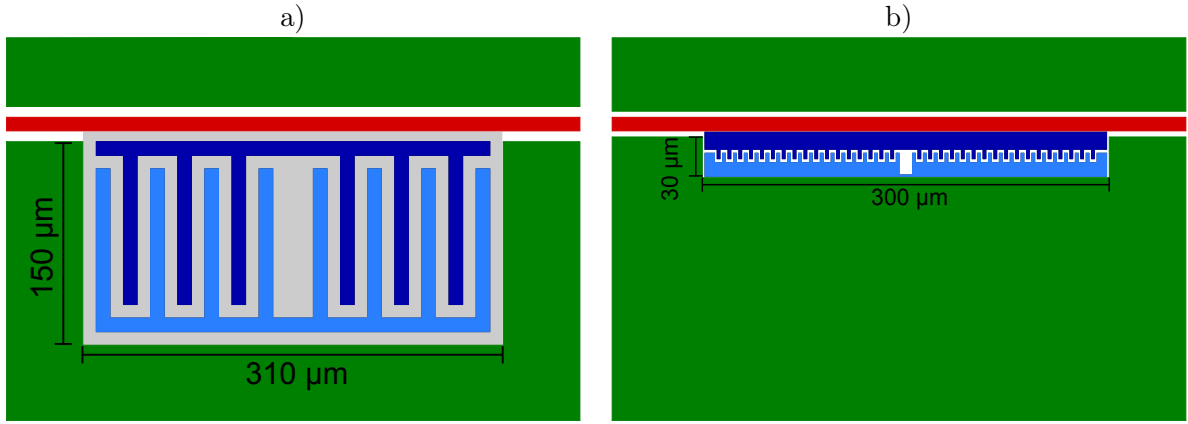


Figure 3.1: a) Approximate reproduction of the transmon design described by ref. [12], used as a starting point for qubit optimization. The gray shaded rectangle indicates the region where the electric field in the surface was calculated. b) Typical transmon design previously used in our group, similar to the qubits described in e.g. ref. [11]. The Josephson junction is not shown, but the resonator (red), island (dark blue), reservoir (light blue) and ground plane (green).

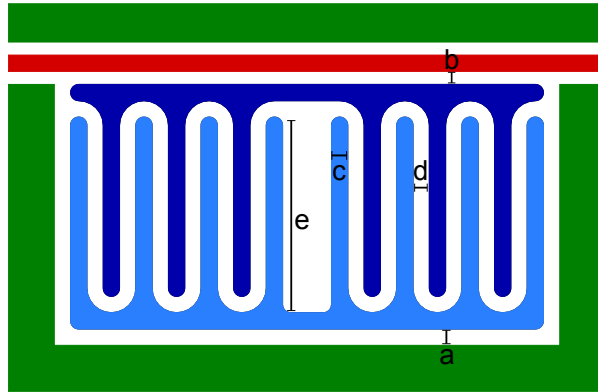


Figure 3.2: Initial parametrized qubit design for optimization based on ref. [12]. The parameters are labelled as: gap reservoir-ground (a), gap resonator-island (b), width of the qubit fingers (c), gap island-reservoir (d) and qubit finger length (e).

3.2 Optimization of transmon parameters

As a starting point for the qubit optimization, the approximate design reported in ref. [12] was used, as shown in Fig. 3.1. In an initial optimization attempt, a number of parameters were introduced: the length of the qubit fingers, their (horizontal) width and the gaps between island-resonator, reservoir-ground and island-reservoir. The (vertical) thickness of the qubit was always kept at 75 nm. Additionally, all corners were replaced by round shapes, since corners locally produce high electric field strengths. The initial parametrized design is shown in Fig. 3.2, with all the parameters indicated.

The main findings of varying these parameters (the results are not shown here, but the simulation files can be found in "Q:\USERS\SimonBur\Maxwell\parameter variations new design\") are:

- Using as many fingers as in the design from ref. [12] combined with a large qubit size increases C_Σ too much, resulting in values for both E_C and g which are clearly below the desired range.
- Decreasing the finger length enormously increases E_c and considerably increases g .

- Small gaps between resonator-island and reservoir-ground strongly increase g , while considerably decreasing E_C .
- Increasing the gap between the island and the reservoir increases E_C and moderately increases g .
- Large gaps decrease the electric field strength in the surface of the substrate.
- Increasing the width of the fingers slightly decreases the electric field in the surface. E_C and g are influenced due to the change in the overall qubit size.

Some of these changes in $E_C \propto 1/C_\Sigma$ can easily be explained by looking at Eq. (2.15): Increasing the capacitance between the island and the reservoir C_{23} (i.e. larger qubit size, longer fingers, smaller gap) decreases E_C .

Some of the changes in $g \propto \beta$ can also be explained by looking at Eq. (2.17),

$$\beta = \frac{C_{12}C_{34} - C_{13}C_{24}}{(C_{12} + C_{24})(C_{13} + C_{34}) + (C_{12} + C_{13} + C_{24} + C_{34})(C_{23} + C_J)} :$$

β is increased if the couplings between island-resonator (C_{34}) and reservoir-ground (C_{12}) are increased, while the couplings between island-ground (C_{13}) and reservoir-resonator (C_{24}) should be decreased, since they contribute to β with a negative sign.

From these considerations, it seemed promising to create new qubits with a large overall size, fewer fingers and an increased gap between the island and the reservoir. The gaps between island-resonator and reservoir-ground form a compromise between a large coupling strength g and small electric fields in the surface of the substrate.

3.3 Intermediate transmon design

For the new final qubit design of this semester project, a new mask for qubit fabrication had to be designed and ordered externally. Until the new mask was received, new qubits for an existing mask were designed, based on previous qubits, as shown in Fig. 3.3. These qubits were designed to increase the coupling g to the desired range by decreasing the gaps island-resonator and reservoir-ground to $1 \mu\text{m}$ (as it was in the old qubit designs), i.e. without taking much compromise regarding the electric field in the surface (previous qubits in Fig. 3.3: $4.5 - 6 \mu\text{m}$). The resulting qubits had similar relaxation times as the previous ones (on the order of $4 \mu\text{s}$), but with increased g . A summary of the qubit properties is given in table A.1.

3.4 Final transmon design

Based on results from numerous simulations, it was decided to design the new mask with cut-outs for the qubits in sizes of $350 \times 150 \mu\text{m}$ (one resonator) and $300 \times 150 \mu\text{m}$ (two resonators), as can be seen in Fig. 3.4. The optimization of the qubit coupling to one resonator is shown as an example in Fig. B.1. An initial parametrized design was created, which seemed promising based on previous simulations. All parameters were then swept across an individual range (restricted by the mask and some of the other parameters). Because the previous (intermediate) qubits with small gaps between island-resonator and reservoir-ground did not increase T_1 as much as we were hoping for, it was decided to increase these gaps again to $4 \mu\text{m}$, at the cost of considerably reducing the coupling strength g , as can be seen in Fig. B.1. In order to slightly compensate for this, an additional extra finger was added to the reservoir, increasing β by an increase in C_{12} . The final qubit design, for both qubits coupled to one and two resonators, is shown in Fig. 3.4.

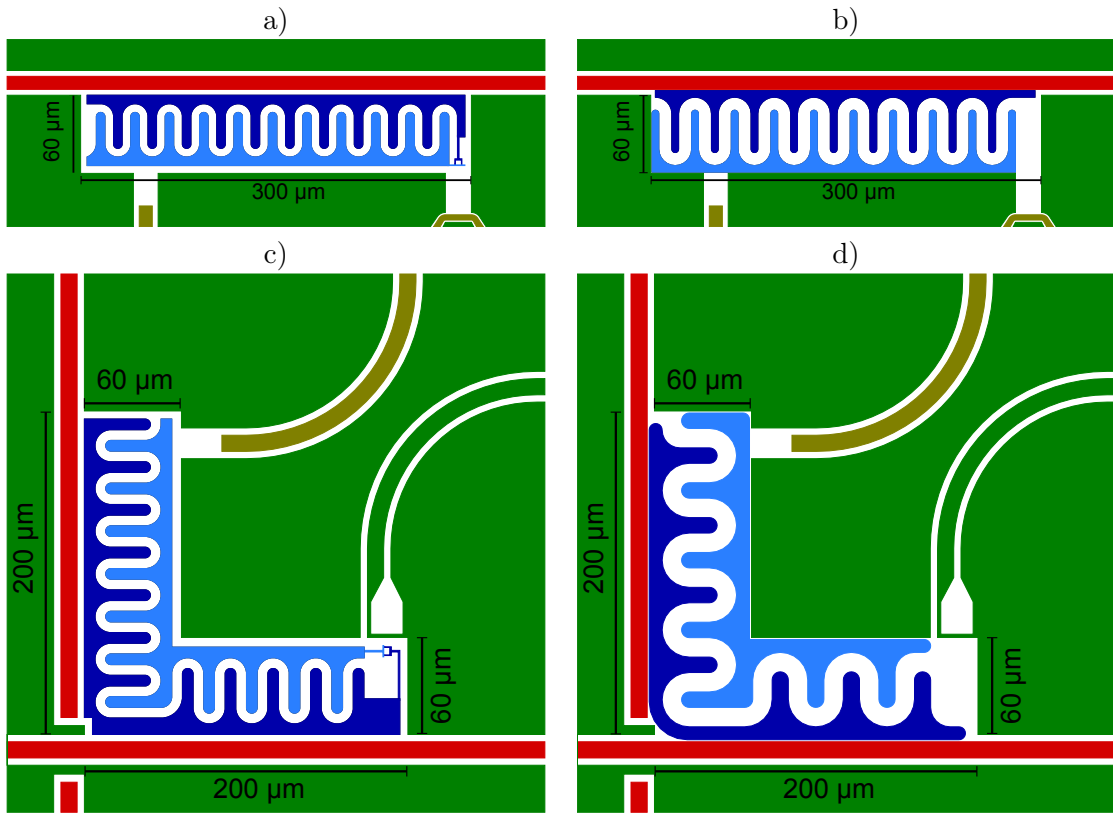


Figure 3.3: Previous qubits, coupled to one resonator (a) and two resonators (c). The split junction is shown here. The charge and flux lines for qubit control are colored brown. Note that for the qubit coupled to two resonators, the flux line is integrated into the ground plane and the seemingly split vertical resonator is connected by a conducting bridge. The new qubits with the previous mask, coupled to one resonator (b) and two resonators (d), were designed to increase g to the desired range.

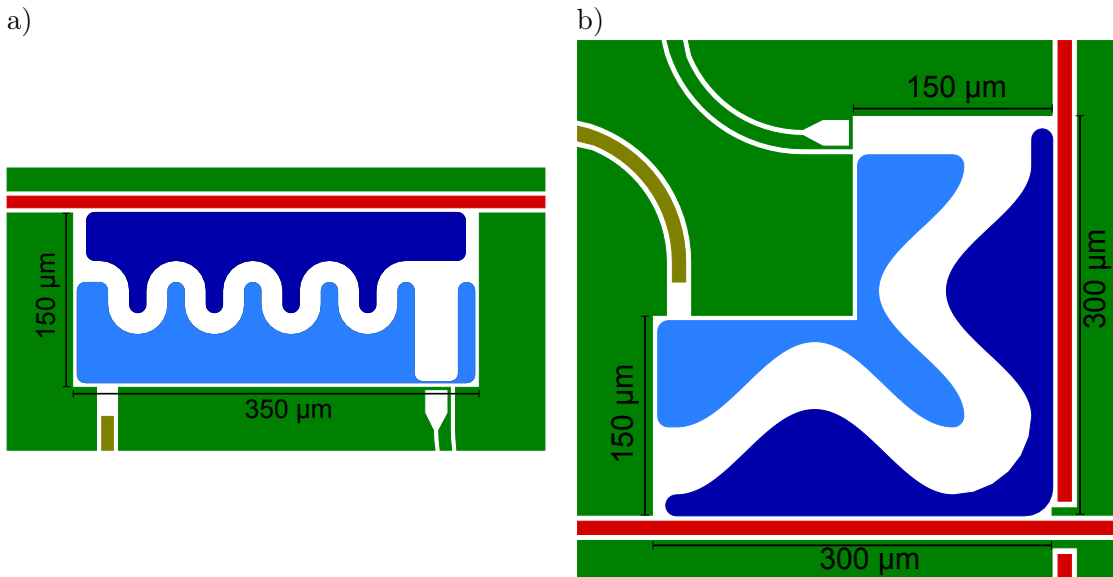


Figure 3.4: Final transmon design of this semester project: a) qubit coupled to one resonator. The additional finger at the right end of the reservoir was added to increase g . b) qubit coupled to two resonators, with a cosine-shaped gap between the island and the reservoir.

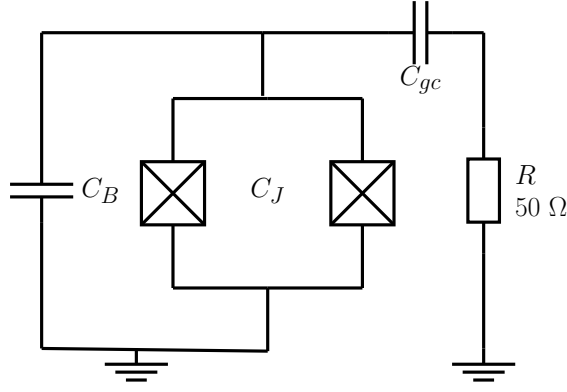


Figure 3.5: Circuit diagram of the simple model for dissipation due to capacitive coupling (C_{gc}) to the charge line with a resistance of 50Ω .

3.5 Comparison of the surface electric field

Despite the lack of a real model for the dielectric loss in the surface of the substrate, the mean electric field in a 5 nm thick surface layer of the substrate was calculated. The results are given in table A.1 for all the qubits mentioned in this report. Plots of a few qubits are shown in Fig. B.2, showing an obvious decrease in the mean electric field strength from the old qubit to the new design. In particular, regions of maximum field strength are strongly reduced.

3.6 Simple estimate of T_1 due to coupling to the charge line

The charge line has a finite resistance which is assumed to be 50Ω . Since the transmon is coupled to the charge line via an effective charge line gate capacitance C_{gc} , dissipation in the charge line contributes to decoherence in the qubit. A simple estimate for the relaxation time due to dissipation in the charge line can be obtained by a classical model following ref. [2], section III E. The transmon circuit can be modelled as an LC-oscillator coupled capacitively to a dissipative element $R = 50 \Omega$, as shown in Fig. 3.5, with $C \approx C_\Sigma$ and $L \approx \hbar^2/4e^2E_J$. The LC-circuit has a classically oscillating charge $Q(t) = Q_0 \cos(\omega t)$ with the oscillator frequency $\omega = q/\sqrt{LC_\Sigma}$. The energy stored in the oscillator is assumed to be on the order of one energy quantum $\hbar\omega$ with $Q_0 = \sqrt{2C_\Sigma\hbar\omega}$. C_{gc} is calculated the same way as C_g for resonators. The voltage across the transmon is given as

$$V(t) = \frac{1}{C_\Sigma}Q(t) = V_0 \cos(\omega t) \quad (3.1)$$

with $V_0 = \sqrt{2\hbar\omega/C_\Sigma}$. The voltage on the island or the reservoir relative to the ground therefore is $V(t)/2$. By using complex notation, i.e. $V(t) = V_0 e^{i\omega t}$, the voltage drop across the impedance R can be calculated from

$$\Re(V_R(t)) = \Re\left(\frac{R}{R + \frac{1}{i\omega C_g}} \frac{1}{2}V(t)\right) = \frac{RV_0 C_g \omega}{2\sqrt{R^2 C_g^2 \omega^2 + 1}} \cos(\omega t) =: V_R^0 \cos(\omega t).$$

With the average power dissipation given as

$$P = \frac{1}{2R} (V_R^0)^2,$$

T_1 can be estimated as

$$T_1 \approx \frac{\hbar\omega}{P}.$$

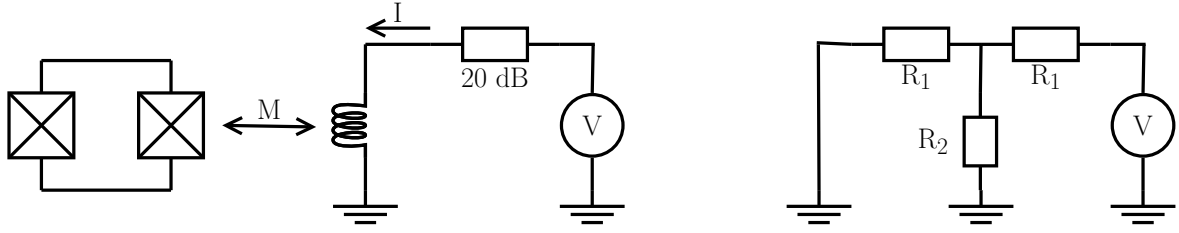


Figure 3.6: Left: schematic network of the coupling between the split junction and the flux line. Right: circuit diagram of the 20 dB attenuator. For $Z_0 = 50 \Omega$, $R_1 = 40.9 \Omega$ and $R_2 = 10.1 \Omega$ are obtained using the online attenuator calculator at <http://www.microwaves101.com/encyclopedia/calccattenuator.cfm>

qubit	ϕ (experiment)	ϕ (simulation)
intermediate mask, old qubit (1 res., Fig. 3.3)	0.1	0.12
intermediate mask, old qubit (2 res., Fig. 3.3)	0.4	0.59
new mask, new qubit (1 res, Fig. 3.4)	0.65	0.76
new mask, new qubit (2 res, Fig. 3.4)	0.55, 0.77	0.79

Table 3.2: Measured and simulated magnetic flux through the split junction loop in units of ϕ_0/V for different qubits. For the new qubit coupled to two resonators, experimental data of two qubits is available.

The resulting estimate for T_1 was $33 \mu\text{s}$ for the final design with the new mask coupled to one resonator, see table C.1. Therefore, T_1 should not be limited by dissipation in the charge line.

3.7 Simulation of the magnetic flux through the split junction

The magnetostatic solver of *Maxwell* can calculate the mutual inductance between conducting loops. This was used to simulate the flux ϕ through the split junction due to a current in the flux line. Since *Maxwell* can only simulate classical behaviour, it can't treat superconductors magnetostatically (they are ignored in the simulation). To replace the superconductors in the simulation, a new material was defined with properties close to a superconductor. The electric conductivity was set to 10^{28} S/m (default for superconductors: 10^{30} S/m) and the relative magnetic permeability to 10^{-10} .

The network is shown in Fig. 3.6. Using the mutual inductance M simulated in *Maxwell*, the magnetic flux ϕ through the junction per voltage V in units of ϕ_0 can be calculated. Some results are shown in table 3.2. The agreement is not perfect, but a reasonable estimate of the flux through the junction can be obtained from the simulation.

4 Conclusion and outlook

The coherence time of our qubits has been improved by a factor of 3-4 by increasing the overall size and modifying the shape of the qubits. However, the increase was smaller than what we initially hoped for, the coherence time reported in ref. [12] could not be achieved. It is currently unclear what the limiting factor for the relaxation time of qubits is. One possibility to further increase the coherence might be an optimization of the qubit production recipe, because optical microscope images of some recently produced qubits showed irregular patterns in the colour of the qubit metal, possibly indicating resist residuals below the qubit metal layer.

Furthermore, a new formula for the coupling strength g was derived. The simulation results obtained using the new formula are in good agreement with experimental data.

Finally, some experience in modelling qubits in *Ansoft Maxwell 14* was obtained, which may be useful for future simulations of related problems.

A Additional tables

qubit	measurement							simulation						
	E_C	ν_{res1}	ν_{res2}	g_1	g_2	$T_1/\mu s$	ref.	# tetr.	E_C	ν_{res1}	ν_{res2}	g_1	g_2	$\langle E \rangle / Vm^{-1}$
old transmon, Fig. 3.1 b)	307	8625	-	340	-	1.1	[13]	748193	323	8625	-	338	-	4.7E+05
intermediate mask, Fig. 3.3 a)	282	7585	-	137	-	4.1	[13]	720963	329	7585	-	151	-	2.7E+05
intermediate mask, Fig. 3.3 c)	251	7585	10070	60	97	4.0	[13]	669690	302	7585	10070	76	106	3.9E+05
intermediate mask, Fig. 3.3 b)	331	8516	-	334	-	$\lesssim 4.5$	[13]	742440	331	8516	-	360	-	2.8E+05
intermediate mask, Fig. 3.3 d)	295	8516	n.a.	318	n.a.	n.a.	[13]	912755	363	8516	9500	180	224	2.2E+05
qubit from ref. [12]	200	7325	-	130	-	9.7	[12]	710991	199	7325	-	121	-	1.9E+05
new mask final design, Fig. 3.4 a)	300	7700	-	260	-	≤ 2.9	[14]	914329	327	7700	-	268	-	9.3E+04
new mask final design, Fig. 3.4 b)	331	8700	9700	n.a.	240	≤ 4.4	[14]	910967	346	8700	9700	204	232	7.8E+04

Table A.1: List of the properties of different qubits: experimental (where available) and simulated values of E_C , g_1 and g_2 , measured relaxation times T_1 (where available) and the calculated mean field $\langle |E| \rangle$ in the surface of the substrate. All energies (E_C , g) and frequencies (ν_{res}) are given in MHz. All experimental T_1 were measured at a drive frequency of approximately 5 GHz.

B Additional figures

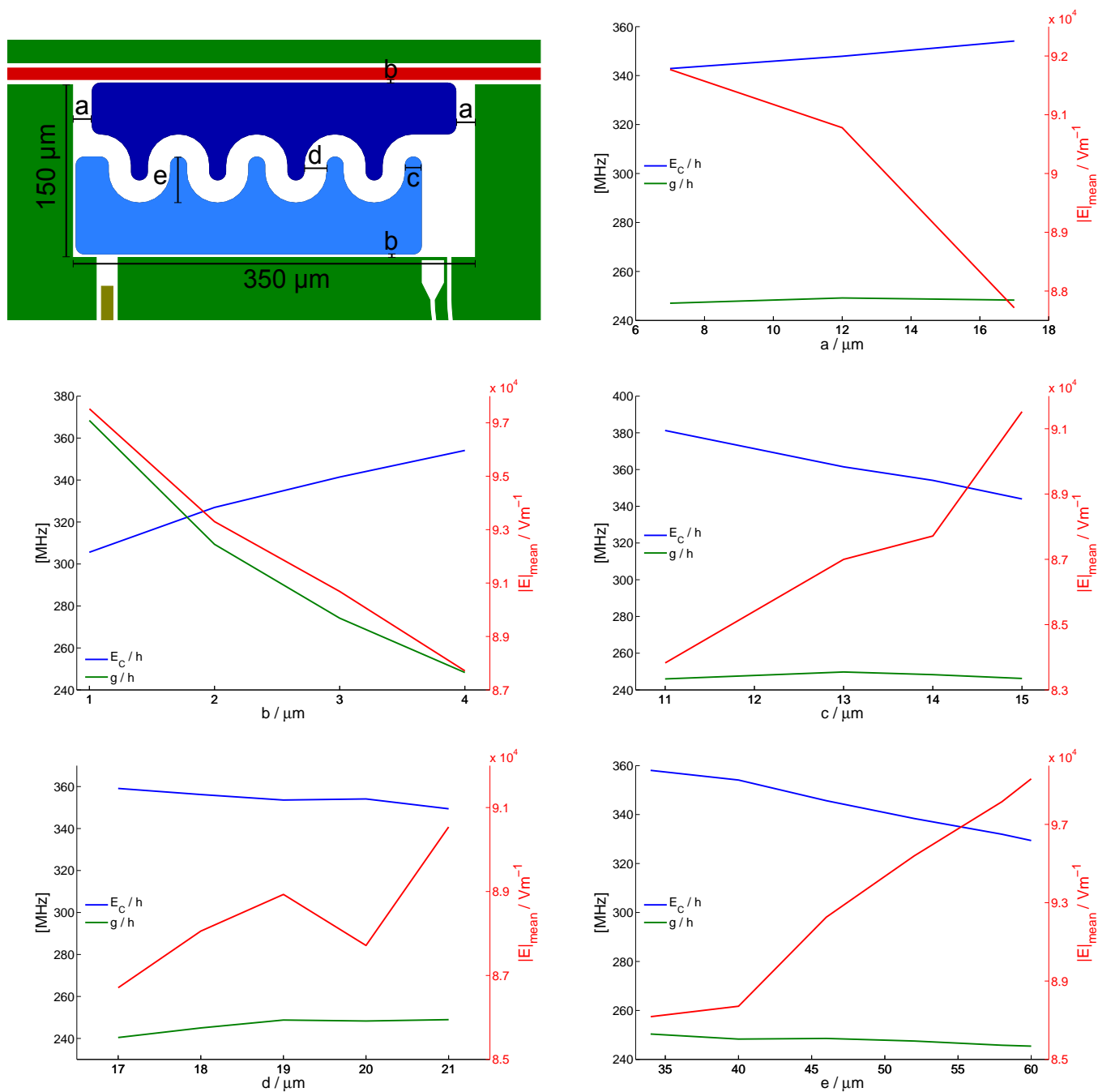


Figure B.1: Example of qubit design optimization by varying geometrical parameters. The plots show the dependence of E_C , g and the mean electric field in the 5 nm surface layer on the design parameters. For the final qubit design, the parameters were chosen as: $a = 12 \mu\text{m}$, $b = 4 \mu\text{m}$, $c = 14 \mu\text{m}$, $d = 19 \mu\text{m}$ and $e = 45 \mu\text{m}$. The resulting qubit is shown in Fig. 3.4, where an additional finger was added to increase g .

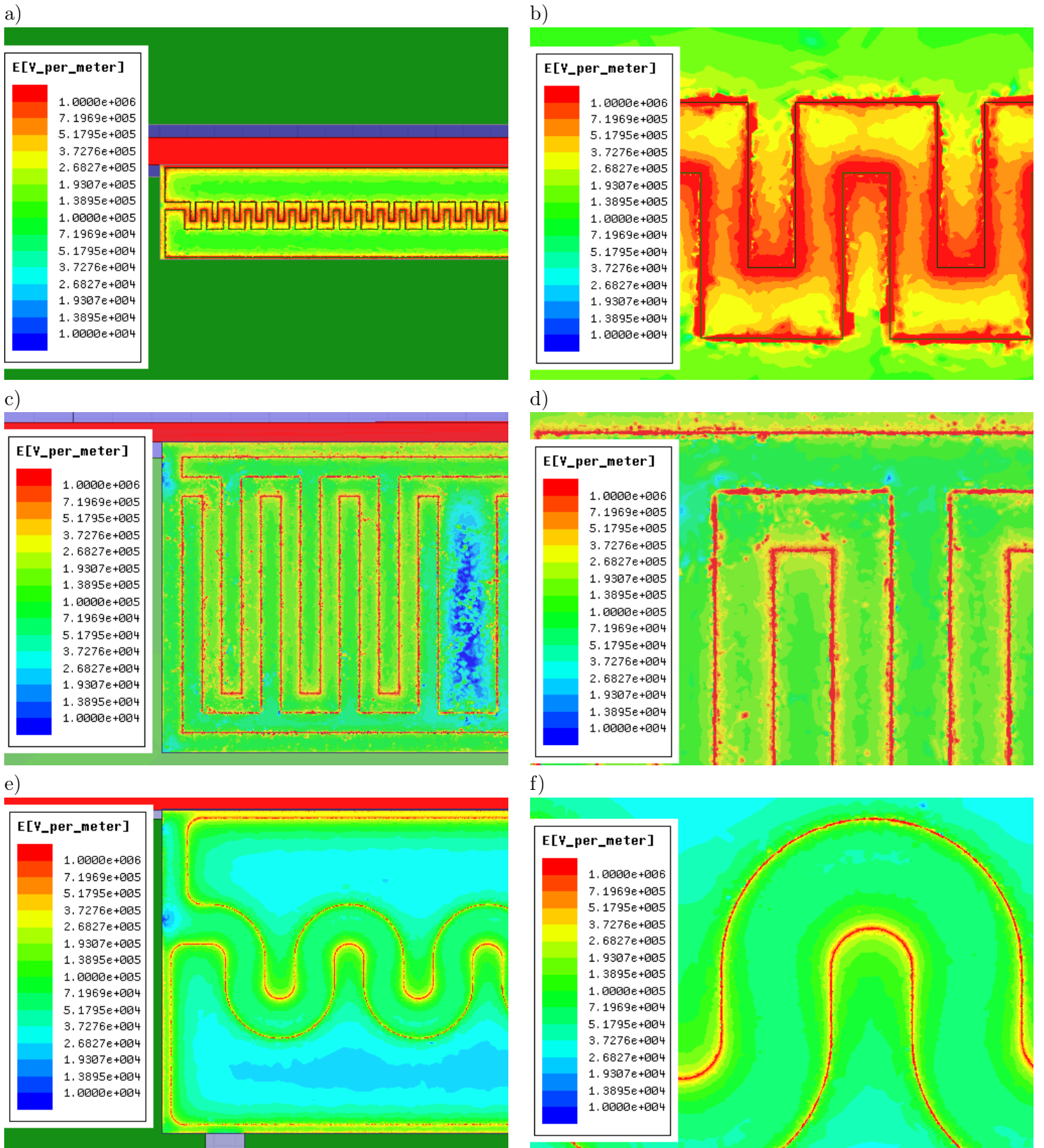


Figure B.2: Plots of the electric field strength on the surface of the substrate for different qubit designs, created with *Maxwell*. In the right column, close-ups of the qubits in the left column are shown. Top to bottom: old qubit design used in ref. [11] ((a), (b)), qubit reported by ref. [12] ((c), (d)), new qubit design ((e), (f)). Note that the field strength is plotted on the same (logarithmic) scale for all qubits, showing a significant decrease in the mean field strength and a particular reduction of regions with very high field strength.

C List of simulation files

The *Maxwell* simulation files of all qubit designs referred to in this report can be found in the folder "Q:\USERS\SimonBur\Maxwell\" (where Q:\ is the "\\windata.ethz.ch\qudev\" folder). The solutions are not contained in this folder, because large mesh files require a lot of disk space (all calculations that were made consumed more than 100 GB in total). If solutions are needed, rerunning a single simulation should not take more than 2 – 3 hours for a parametric design, and less than one hour for a single geometry. A list of the file names used for the qubits described in this report is given in table C.1.

qubit	path (Q:\USERS\SimonBur\Maxwell\...)
typical old qubit, as used in ref. [11]	standard transmon\finalM14Q1.mxwl
qubit reported in ref. [12]	IBM_Chow12\IBM_Chow12.mxwl
previous qubits with intermediate mask (Fig. 3.3)	Mask20_K1v6\Mask20_K1v6_lowerleft.mxwl (1 resonator) Mask20_K1v6\Mask20_K1v6_upperleft.mxwl (2 resonators)
new qubits with intermediate mask (Fig. 3.3)	old mask qubit 1\oldmask_qubit1_new.mxwl (1 resonator) old mask qubit 2\oldmask_qubit2_final_produced.mxwl (2 resonators)
parametric optimization with new mask (Fig. B.1)	Mask23_qb1\Mask23_qb1_sweep_*.mxwl
new qubits with new mask (Fig. 3.4)	Mask23_qb1\Mask23_qb1_3.mxwl (1 resonator) Mask23_qb2\wave\Mask23_qb2_wave_optimized.mxwl (2 resonators)
flux coupling simulations (table 3.2)	fluxline\Mask20_K1v6_lowerleft_fluxline.mxwl fluxline\Mask20_K1v6_upperleft_fluxline.mxwl fluxline\Mask23_qb1_3_fluxline.mxwl fluxline\Mask23_qb2_wave_optimized_fluxline.mxwl

Table C.1: List of the file names used for the qubit simulation files. The path for all files starts with "Q:\USERS\SimonBur\Maxwell\".

D *Maxwell* "manual"

The purpose of this section is to give a short description on how to calculate the quantities used in this semester project with *Ansoft Maxwell 14*.

D.1 General

When a new *Maxwell* file is opened, click *Project > Insert Maxwell 3D Design*. Before starting to draw objects, it is recommended to choose the length unit of the drawing (*Modeler > Units*) and specify the solution type (*Maxwell 3D > Solution Type*) to either *Electrostatic* for calculating electric fields and the capacitance matrix or *Magnetostatic* for calculating magnetic fields and the inductance matrix. Then all the objects can be drawn either by hand or imported from CAD files (described below). At some point, a vacuum box surrounding all objects has to be drawn, defining the problem region in which to solve Maxwell's equations.

D.2 Import and export CAD drawings

Maxwell can import different CAD file types using *Modeler > Import*, including *AutoCAD* files (.dwg and .dxf). However, files created in *AutoCAD 2010* could not be imported directly to *Maxwell 14* due to incompatible file formats. As a workaround, .dxf files created with *AutoCAD 2012* can be converted to GDSII files (.gds) using *LinkCAD 5*, which can be imported into *Maxwell*.

When a 2D CAD drawing is imported, Maxwell creates 2-dimensional sheets. These can be made 3-dimensional by selecting the objects and clicking *Modeler > Surface > Thicken Sheet* and choosing the desired thickness.

Drawings created in *Maxwell* can easily be exported to .dxf files by clicking *Modeler > Export*. This always worked fine, the exported files could be opened in *AutoCAD 2012* without problems.

D.3 Excitations, Matrix, Solution Setup

Maxwell needs at least one *Excitation* (boundary condition) assigned to an object to solve the problem, otherwise, there is nothing to solve. The available excitations depend on the solution type. For the electrostatic solution, possible excitations include voltage, charge or charge density. To define an excitation, right-click an object and choose *Assign Excitation > ...*. Matrices such as the capacitance matrix can only be calculated for objects with excitations, so an excitation must be assigned to every object of interest. Excitations can be zero, but simulations normally converge better if some nonzero excitations are assigned. The capacitance matrix does not depend on the value of the excitations, but fields do of course.

To define the capacitance matrix (after assigning excitations in the electrostatic solution type), click *Maxwell 3D > Parameters > Assign > Matrix*, then check the objects which should be included in the capacitance matrix.

Finally, a solution setup has to be defined. Click *Maxwell 3D > Analysis Setup > Add Solution Setup... .* Choose a *Maximum Number of Passes* (to just check if the simulation works, choose a small number) click ok, and the simulation can be started. After the simulation, information about the mesh size, convergence and the capacitance matrix can be found in *Maxwell 3D > Results > Solution Data... .*

D.4 Output variables, field calculator, reports

Output variables are a useful tool to directly let *Maxwell* calculate functions of quantities like capacitances or field operations. Output variables can be defined in *Maxwell 3D > Results > Output Variables*.

The field calculator (*Maxwell 3D > Fields > Calculator...*) can perform operations on the electric field of the solution, such as integrating the field over objects of the design. Integrals can only be performed on objects which are modelled in the simulation, non-model objects produce an error message. In the calculator, expressions can be saved and used in the definition of output variables.

To create a report, click *Maxwell 3D > Results > Create Electrostatic/Fields Report > ...* and choose the quantities which should be written in a table or plotted. The reports can be found in *Results* in the *Project Manager*.

D.5 Design Parameters

To add a parameter to an object, first draw the object with some arbitrary size. Then double-click the object (the command for creating the object, e.g. *CreateBox* for a box) in the history tree to see the coordinates and dimensions of the object. Now, a variable can be added by simply typing it into the coordinates or dimensions. A little window *Add Variable* will show up, where the name (some names are protected), unit and value of the variable can be defined. Alternatively, variables can be defined in *Maxwell 3D > Design Properties* (click *Add...*). Created variables are listed and can be edited in *Maxwell 3D > Design Properties*. Note: the coordinates and dimensions of objects can be defined as formulas containing both variables and constant numbers. However, if variables and constant numbers are used, always add the correct units to the numbers, e.g. "1 um + a" instead of "1 + a". Otherwise, *Maxwell* will create a mess by interpreting units wrongly, for instance "1 + a" may be interpreted as "1 m + a", even if the units of the drawing are specified as um (micrometers).

Design parameters can be animated, which can be very useful to check the drawing for errors if a large number of objects are created with complicated dependence on several variables. To do so, click *View > Animate* and choose the variable and the range for animation.

To get *Maxwell* to simulate the design for different values of some parameter, click *Maxwell 3D > Optimetrics Analysis > Add Parametric...* Note that this will only work after the rest of the simulation setup is finished. A window *Setup Sweep Analysis* will pop up. Click *Add..* to add a sweep definition. Afterwards, the parameter variations are listed in the tab *Table* of the *Setup Sweep Analysis* window. Go to the tab *Options* and check *Save Fields and Mesh*, if you want *Maxwell* to evaluate expressions depending on field operations. If this box is left unchecked, only the mesh and field of the reference design (the value of the parameter listed in *Maxwell 3D > Design Properties*) will be saved. This also means that if you want to increase the accuracy of the results by increasing the number of passes after a first completion of the simulation, the simulation for each value of the parameter except the reference design will restart from the beginning. So this box should always be checked, unless hard disk space is strongly limited.

Output variables can be written in tables or plotted as a function of the sweep parameter by clicking *Maxwell 3D > Results > Create ... Report > Rectangular Plot / Data Table* and choosing the parameter as *Primary Sweep*.

D.6 Magnetostatic solution

To calculate the inductance matrix, currents have to be assigned to the objects of interest, which should be closed conducting loops, otherwise, the simulation may sometimes stop and produce an error message. However, the current excitation can only be assigned to 2-dimensional surfaces (the current is defined to be perpendicular to the surface), therefore, to assign a current to a 3-dimensional object (such as the flux line), the current excitation has to be defined on a 2-dimensional sheet which is placed inside the conductor. This can be achieved by intersecting the conductor with a rectangle. To do so, click *Modeler > Grid Plane > ...* and select the plane which is perpendicular to the current at the position where the current excitation shall be defined. Draw a rectangle (*Draw > Rectangle*) which intersects the entire cross section of the conductor. Copy the conductor, select the sheet and the copied conductor and click *Modeler > Boolean > Intersect*. The current excitation can now be assigned to the resulting intersection of the conductor and the sheet (*Maxwell 3D > Excitations > Assign > Current*). The direction of the current and its magnitude can be chosen (choose a nonzero current for better convergence).

Once a current excitation is defined on all objects of interest, the inductance matrix can be defined in the same way as the capacitance matrix (*Maxwell 3D > Parameters > Assign > Matrix*). The rest (solution setup) is the same as described above.

Acknowledgements

I would like to express my thanks to Prof. Dr. Andreas Wallraff for giving me the opportunity to do this semester project in his group, to Dr. Arkady Fedorov for the supervision of the project, useful discussions and lots of information, to Lars Steffen for interesting information and instructions in the lab and technical support, and to the entire Qudev group for a good time.

References

- [1] R. J. Schoelkopf, and S. M. Girvin, *Nature* **451**, 664 (2008).
- [2] J. Koch, T. M. Yu, J. Gambetta, A. A. Houck, D. I. Schuster, J. Majer, A. Blais, M. H. Devoret, S. M. Girvin, and R. J. Schoelkopf, *Phys. Rev. A* **76**, 042319 (2007).
- [3] J. M. Fink, *Quantum Nonlinearities in Strong Coupling Circuit QED*, Diss. ETH No. 19299 (2010).
- [4] M. H. Devoret, *Quantum fluctuations in electrical circuits*. In S. Reynaud, E. Giacobino & J. Zinn-Justin, eds., Les Houches Session LXIII, *Quantum Fluctuations*, pp. 351-386. Elsevier (1997).
- [5] M. Büttiker, *Phys. Rev. B*, **36**, 3548 (1987).
- [6] V. Bouchiat, D. Vion, P. Joyez, D. Esteve, and M. H. Devoret, *Phys. Scr.* **T76**, 165 (1998).
- [7] B. D. Josephson, *Phys. Lett.* **1**, 251 (1962).
- [8] J. M. Martinis, K. B. Cooper, R. McDermott, Matthias Steffen, Markus Ansmann, K. D. Osborn, K. Cicak, Seongshik Oh, D. P. Pappas, R.W. Simmonds, and C. C. Yu, *Phys. Rev. Lett.* **95**, 210503 (2005).
- [9] C. Mueller, A. Shnirman, and Yu. Makhlin, *Phys. Rev. B* **80**, 134517 (2009).
- [10] J. Wenner, R. Barends, R. C. Bialczak, Yu Chen, J. Kelly, Erik Lucero, Matteo Mariantoni, A. Megrant, P. J. J. O'Malley, D. Sank, A. Vainsencher, H. Wang, T. C. White, Y. Yin, J. Zhao, A. N. Cleland, and J. M. Martinis, *Appl. Phys. Lett.* **99**, 113513 (2011).
- [11] M. Baur, A. Fedorov, L. Steffen, S. Filipp, M. P. da Silva, and A. Wallraff, *Phys. Rev. Lett.* **108**, 040502 (2012).
- [12] J. M. Chow, J. M. Gambetta, A. D. Córcoles, S. T. Merkel, J. A. Smolin, C. Rigetti, S. Poletto, G. A. Keefe, M. B. Rothwell, J. R. Rozen, M. B. Ketchen, and M. Steffen, *arXiv:1202.5344v1* (2012).
- [13] M. Peterer, *Investigating the suppression of external sources of decoherence in transmon qubits*, Master Thesis, ETH Zürich, 2012
- [14] *Current stage of quantum teleportation*, internal document (unpublished).